JACS
JOURNAL OF THE AMERICAN CHEMICAL SOCIETY

Article

pubs.acs.org/JACS

Visualizing the Molecular Recognition Trajectory of an Intrinsically Disordered Protein Using Multinuclear Relaxation Dispersion NMR

Robert Schneider,[†,‡,§,∥] Damien Maurin,[†,‡,§] Guillaume Communie,[†,‡,§] Jaka Kragelj,[†,‡,§] D. Flemming Hansen,[⊥] Rob W. H. Ruigrok,[#,∇,○] Malene Ringkjøbing Jensen,[†,‡,§] and Martin Blackledge*[,†,‡,§]

[†]University of Grenoble Alpes, IBS, 38044 Grenoble, France

[‡]CNRS, IBS, 38044 Grenoble, France

[§]CEA, IBS, 38044 Grenoble, France

[⊥]Institute of Structural and Molecular Biology, Division of Biosciences, University College London, Gower Street, London WC1E 6BT, United Kingdom

[#]Univ. of Grenoble Alpes, UVHCI, 38000 Grenoble, France

[∇]CNRS, UVHCI, 38000 Grenoble, France

[○]Unit for Virus Host-Cell Interactions, Univ. of Grenoble Alpes-EMBL-CNRS, 38000 Grenoble, France

Supporting Information

ABSTRACT: Despite playing important roles throughout biology, molecular recognition mechanisms in intrinsically disordered proteins remain poorly understood. We present a combination of $^{1}H^{N}$, $^{13}C'$, and ^{15}N relaxation dispersion NMR, measured at multiple titration points, to map the interaction between the disordered domain of Sendai virus nucleoprotein (NT) and the C-terminal domain of the phosphoprotein (PX). Interaction with PX funnels the free-state equilibrium of NT by stabilizing one of the previously identified helical substates present in the prerecognition ensemble in a nonspecific and dynamic encounter complex on the surface of PX. This helix then locates into the binding site at a rate coincident with intrinsic breathing motions of the helical groove on the surface of PX. The binding kinetics of complex formation are thus regulated by the intrinsic free-state conformational dynamics of both proteins. This approach, providing high-resolution structural and kinetic information about a complex folding and binding interaction trajectory, can be applied to a number of experimental systems to provide a general framework for understanding conformational disorder in biomolecular function.

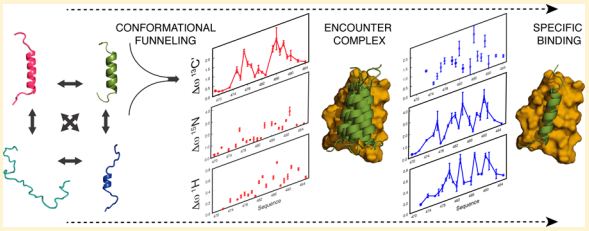

INTRODUCTION

Intrinsically disordered proteins (IDPs) are abundant throughout biology,[1−4] in particular, in eukaryotic proteomes and in some viruses,[5] playing crucial roles, for example, in signaling pathways or regulation of transcription and replication.[6] Biological function of IDPs is often mediated by short sequences of peptides, known as linear motifs, that control a vast range of cellular processes through interactions with structured partner proteins.[7,8] In spite of the ubiquitous nature of IDPs, the exact molecular mechanisms regulating their interactions with physiological partners remain poorly understood. This is of prime importance because many IDPs are involved in human disease.[9] The development of rational pharmacological strategies awaits a detailed understanding of the molecular basis of biological interaction and function in this extensive but poorly understood fraction of the human proteome. IDPs exhibit highly heterogeneous local and long-range structural and dynamic propensities, and this sequence-dependent conformational behavior is thought to play a key role in regulating function. Considerable effort has therefore been devoted to the development of robust approaches to describe conformational heterogeneity in IDPs[10−16] and its relationship to functional properties such as recognition of physiological partners.[17−20]

The relationship between free- and bound-state conformational behavior is however not straightforward,[21] as exemplified by the observation of promiscuous IDPs adopting distinct conformations of the same binding sites in complex with different interaction partners.[22] Depending on the relative importance of enthalpic and entropic contributions, either prefolded or unfolded forms may be considered more likely to mediate binding via conformational selection or induced-fit-type interactions.[23−26] The mechanisms underpinning the kinetics of IDP interactions are rendered yet more complex by the suggestion that some complexes involving IDPs remain dynamic even in interaction with their partners.[27] Although a growing body of theoretical,[28−31] numerical,[32−35] and kinetic studies[36−38] have been used to predict or globally characterize

Received: October 28, 2014
Published: December 31, 2014

DOI: 10.1021/ja511066q
J. Am. Chem. Soc. 2015, 137, 1220−1229

molecular recognition in IDPs, these processes remain largely unexplored at atomic resolution.[39]

NMR studies of interactions involving IDPs are frequently hampered by excessive line broadening, because exchange between free and bound conformations often occurs on timescales that give rise to intermediate exchange broadening (in the millisecond range), precluding direct detection of the bound-state peaks. It is possible to investigate the origin of this line broadening, by detecting the free state, at low titration admixtures of the partner protein, where the resonances are only weakly broadened. Under these conditions, where the bound state represents a weakly populated minor state, relaxation dispersion (RD) NMR[40,41] can be used to investigate the structure, population, and interconversion rates of the otherwise invisible bound-state equilibrium.[17]

In this study we use RD, measured for multiple nuclei (^{15}N, ^{13}C′, and ^{1}H^{N}) and at multiple admixtures of the intrinsically disordered C-terminal domain of Sendai virus nucleoprotein (NT, residues 401−524) and the partially folded C-terminal headgroup of the phosphoprotein (PX, residues 474−568), to develop a detailed description of the trajectory from the free state equilibrium to the bound state. Changes in ^{13}C chemical shifts predominantly report on changes in secondary structure formation,[42] while changes in ^{15}N and ^{1}H shifts are particularly sensitive to the tertiary interactions formed at the binding interface of two proteins. The combination of these complementary sources of information proves to be crucial for describing the intricate interaction pathway.

Sendai virus belongs to the paramyxoviridae genus, within which the important human pathogens Measles, Nipah, and Hendra share homologous PX and NT domains.[43,44] The NT:PX interaction in this viral family is thought to play an essential role in replication in vivo in initiating the interaction between the viral polymerase and the genome.[45] The NT:PX interaction is central to the viral replication machinery and as such represents an important and viable target for rational drug design in this class of viruses.

We previously used NMR residual dipolar couplings to characterize the conformational equilibrium of unbound NT, revealing an interaction site sampling three distinct, differently populated N-capped[46] helical substates, in rapid exchange with a completely unfolded population.[47,48] This linear motif is thought to further fold upon binding to PX[49] on the basis of the crystal structure of a chimeric construct of the homologous NT:PX complex from Measles virus.[50,51] NT is an ideal system with which to investigate folding and binding interactions, because of the detailed understanding of the intrinsic conformational sampling of the free form of the protein. Our aim is to map the entire interaction trajectory to determine whether the nature of the free-state ensemble, in particular, the different prefolded helical conformations, plays any role in the molecular recognition process.

RESULTS

NMR Relaxation Dispersion Studies of the NT:PX Interaction. NMR chemical shift titration studies of the NT:PX complex show that resonances of NT from throughout the interaction region (residues 473−492) experience line broadening (Figure S1, Supporting Information). In this exchange regime NMR titration only provides an estimate of the dissociation constant K_d < 60 μM.[49] We therefore carried out isothermal titration calorimetry (ITC) measurements, which allow a more precise determination of the dissociation constant, K_d = 8.4 ± 0.9 μM (Figure S2, Supporting Information). In order to identify the molecular mechanisms giving rise to the observed broadening of the NT resonances, ^{15}N, ^{13}C′, and ^{1}H^{N} RD experiments were performed on NT (401−524) at two magnetic fields (14.1 and 18.8 T) and at admixtures ranging from 0 to 0.15 molar ratios of PX (see Experimental Section). No detectable RD is measured in free NT (Figure S3, Supporting Information), confirming the rapid nature of the exchange between the three helical substates and the unfolded state. However, even at the smallest PX:NT molar ratio (0.02), RD is measured throughout the previously identified[47,49] molecular recognition element for all three types of nuclei (Figures 1 and S4, Supporting Information). No exchange is

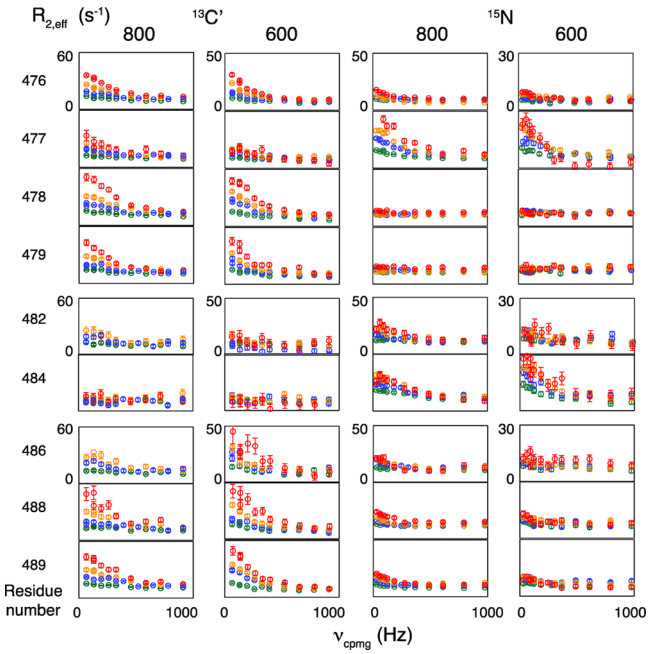

Figure 1. ^{13}C and ^{15}N $R_{2,eff}$ RD curves for selected residues measured on NT at 14.1 and 18.8 T (600 and 800 MHz ^{1}H Larmor frequency) for 2% (green), 3.5% (blue), 5% (orange), and 8% (red) molar ratio admixtures of PX:NT. Data from the 15% admixture and ^{1}H^{N} data are not shown in the interest of space. Residue number i refers to the peptide plane containing the amide group of residue i and the carbonyl carbon of residue i − 1.

detectable using RD from residues outside the helical region for any admixture. We note that most resonances from the molecular recognition element are broadened beyond detection at PX:NT molar ratios higher than 0.20 (Figure S5, Supporting Information).

More than 700 experimental RD curves were measured from throughout the molecular recognition element. Examination of the measured dispersion curves reveals a complex distribution with clear differences in exchange contributions to the effective transverse relaxation rate ($R_{2,eff}$) from the different nuclei for distinct peptide units. For example, while backbone carbonyl groups experience continuous exchange contributions between residues 474−479 and 486−492, the central section of the helical region, comprising residues 480−484, exhibits weaker ^{13}C′ dispersion and larger ^{15}N exchange contributions (Figure 1).

Analysis of RD Data from the Molecular Recognition Element in Terms of a Two-State Binding Model. Data were analyzed using the following approaches: First, for each titration admixture all data from each individual peptide plane (^{15}N and ^{1}H^{N} of residue i and ^{13}C′ of residue i − 1) in the

DOI: 10.1021/ja511066q
J. Am. Chem. Soc. 2015, 137, 1220−1229

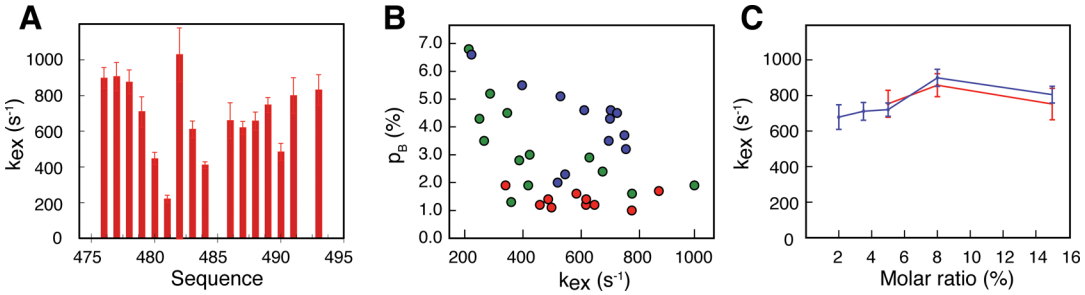

Figure 2. Kinetic parameters derived from analysis of RD data using a two-state model. (A) Exchange rates (k_{ex}) determined from $^{1}H^{N}$, $^{13}C'$, and ^{15}N RD curves for individual residues in the PX interaction region of NT, fitting admixtures containing 2%, 3.5%, 5%, and 8% PX simultaneously using the Carver–Richards expression for two-state exchange (Figure S7, Supporting Information). (B) Residue- and admixture-specific exchange rates k_{ex} and bound-state populations p_B for residues in the PX binding site of NT, color-coded by admixture (red 2%, green 3.5%, blue 5% PX), obtained by numerical fits of individual residue $^{1}H^{N}$, $^{13}C'$, and ^{15}N RD data at individual admixtures to a two-state exchange model (Figure S6, Supporting Information). (C) Dependence of k_{ex} values on molar ratio. (Blue) k_{ex} measured for NT with respect to [PX]:[NT] molar ratio. k_{ex} values were obtained from global fits of a two-state exchange model to NT $^{13}C'$, ^{15}N, and $^{1}H^{N}$ RD data from all residues at individual titration mixtures. The blue curve can be fit using a constant k_{ex} = 771 ± 38 s^{-1}. (Red) k_{ex} measured on PX with respect to [NT]:[PX] molar ratio. k_{ex} was obtained from global fits of a two-state exchange model to ^{15}N and $^{1}H^{N}$ RD data from all residues on PX exhibiting exchange in the presence of NT but not in the absence of NT. This curve can be fit with a constant value of k_{ex} = 803 ± 37 s^{-1}.

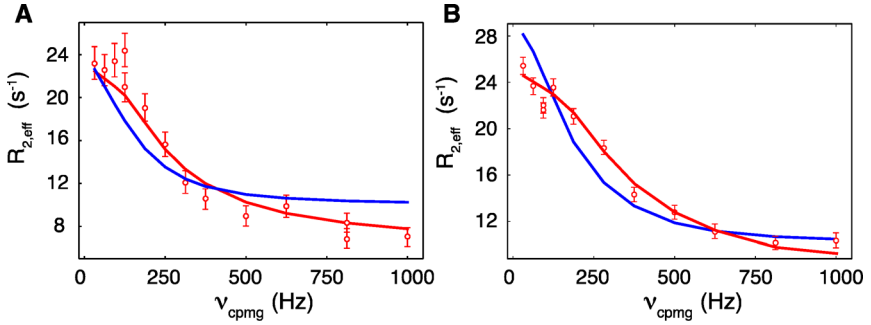

Figure 3. Examples of the improvement in the reproduction of RD data from some sites when fitting all data from a single admixture assuming a single global two-state exchange process and when fitting all data from a single admixture assuming a single global three-state kinetic model. Experimental ^{15}N RD data (red points) are shown for residue 484, for the 5% PX:NT admixture (blue: two-state fit, as shown in Figure S8, Supporting Information, red: three-state fit as shown in Figure 4). Left-hand figure shows data measured at 14.1 T and right-hand figure shows data measured at 18.8 T.

interaction region were analyzed using a two-state exchange model[52,53] to determine the chemical shift differences ($\Delta\omega$) between the free form and the bound state, the residue-specific exchange rates (k_{ex}), and the bound state populations (p_B) (Figure S6, Supporting Information). The analysis was repeated, this time simultaneously analyzing all data for each individual peptide plane at titration admixtures from 2% to 8% admixtures of PX, assuming residue-specific exchange rates (Figure S7, Supporting Information). In both cases a nonuniform k_{ex} is observed along the primary sequence, with rates in the 474–478 and 486–489 range clustering between 700 and 800 s^{-1} and residues in the central region exhibiting higher or lower rates (Figure 2A). This variability of k_{ex} is associated with a nonuniform distribution of p_B values (Figure 2B). Importantly, simultaneous analysis of all data at individual titration mixtures using common k_{ex} and p_B values also demonstrates that while the majority of curves are reproduced by k_{ex} of 771 ± 38 s^{-1} (Figure S8, Supporting Information) a number of curves, in particular, those showing large ^{15}N dispersion, are very poorly reproduced (representative examples shown in Figure 3).

Analysis of RD Data from the Molecular Recognition Element in Terms of a Three-State Binding Model. The observation of heterogeneous exchange rates and populations over the interaction region and the inability of a global two-state exchange approach to acceptably reproduce all experimental data suggest that this model is insufficient to explain the NT:PX interaction. We therefore tested linear three-state exchange models (see Experimental Section). Although the parametric space available from such a three-state fit is ill defined, inherent degeneracy is raised by the combination of the $^{13}C'$, ^{15}N, and $^{1}H^{N}$ RD data. As an example, the most complete data set, measured at 0.05 PX:NT ratio, provides a convergent fit to a linear exchange model, yielding a global minimum centered around $k_{ex,AB}$ = 852 ± 31 s^{-1} and $k_{ex,BC}$ = 2600 ± 493 s^{-1}, with p_B = 3.7 ± 0.1% and p_C = 1.3 ± 0.1% (Figures 4 and S9, Supporting Information). RD data measured at the other individual admixtures are closely consistent with this model (Figure 4). Improvement in data reproduction (Figure 3, Table 1) using the more complex model is statistically significant for all individual molar ratios (p < 0.0001 at [PX]/[NT] = 0.05, 0.08, and 0.15; p < 0.01 at [PX]/[NT] = 0.35, Table 1) with the exception of [PX]/[NT] = 0.02, probably due to the low amplitude of the RD phenomena at this admixture. Equally importantly, fitted p_B and p_C values for admixtures other than 5% fall closely within the range expected from the K_d of the interaction (Figures 5 and S10, Supporting Information). A combined analysis fitting admixtures from 2% to 8% simultaneously using a global three-state model resulted in $\Delta\omega_{AB}$ and $\Delta\omega_{AC}$ values as well as kinetic and thermodynamic parameters similar to those obtained from the individual

DOI: 10.1021/ja511066q
J. Am. Chem. Soc. 2015, 137, 1220–1229

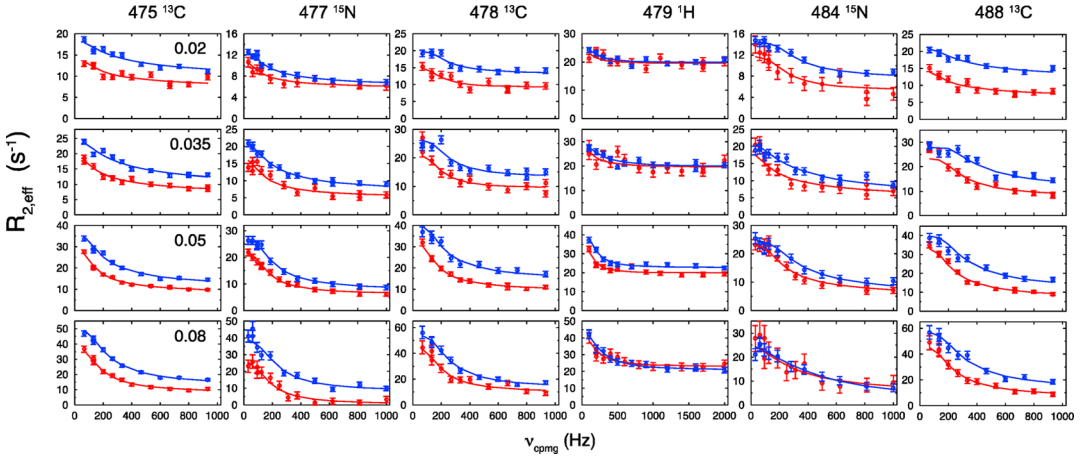

Figure 4. Three-state characterization of the NT:PX interaction from RD. Examples of fits to RD curves from NT. $^{1}H^{N}$, $^{13}C'$, and ^{15}N data from all peptide planes in the PX interaction region of NT were simultaneously fitted by numerical integration of the Bloch−McConnell equations for three-state exchange, separately for different admixtures. Fixed rates $k_{ex,AB}$ and $k_{ex,BC}$ were used, with $k_{ex,AB}$ varying between 827 and 948 s^{-1} as appropriate for the varying concentrations of free PX in the different admixtures, and $k_{ex,BC}$ = 2600 s^{-1} constant (see Experimental Section): solid lines, fitted curves; circles, data points (red, 14.1 T; blue, 18.8 T). A 3D plot of the same data is found in Figure S9, Supporting Information. 3-state simultaneous fitting of all data from 2% to 8% resulted in very similar $\Delta\omega_{AB}$ and $\Delta\omega_{AC}$ values and k_{AB} = 884 ± 99 s^{-1} and k_{BC} = 2374 ± 590 s^{-1} for the 5% admixture (Figure S11, Supporting Information).

Table 1. Comparison of Goodness of Fit Parameters for the Global Two-State and Global Three-State Fits of Data Measured from NT at Each Different Admixture of PX[a]

admixture	N data	N(param) 2 state	N(param) 3 state	χ^2 2 state	χ^2 3 state	*F* test	*P*
2.0%	678	101	134	526.30	488.80	1.265	0.16
3.5%	726	101	134	740.50	677.51	1.668	0.01
5.0%	609	89	118	534.49	456.46	2.894	<0.0001
8.0%	556	80	106	420.54	353.60	3.276	<0.0001
15.0%	447	65	86	479.36	399.81	3.420	<0.0001

[a]In all cases except for the 2.0% admixture the three-state fit is significantly better than the two-state fit. The lack of significance in improvement for this admixture is probably due to signal to noise, related to the small amplitude of the RD effects at the lowest admixture.

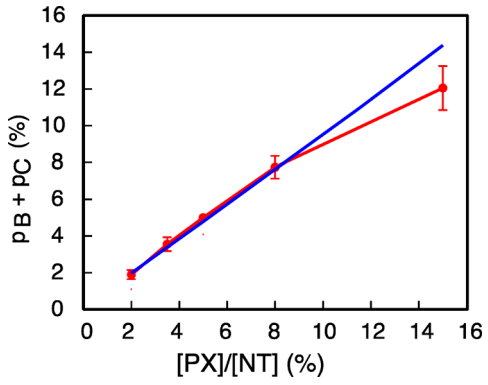

Figure 5. Population of the PX-bound form of NT for the different PX:NT admixtures determined from analysis of RD data. Solid red line shows the fitted (p_B + p_C) values from the consensus three-state fit shown in Figure 4. Note that for the 5% data set p_B + p_C was fixed to 5% as described in the Experimental Section. Blue line indicates the calculated p_B assuming a dissociation constant of 8.4 ± 0.9 μM as estimated from ITC measurements (Figure S2, Supporting Information).

admixtures (Figure S11, Supporting Information, $k_{ex,AB}$ = 884 ± 99 s^{-1} and $k_{ex,BC}$ = 2374 ± 590 s^{-1}, p_B = 3.3 ± 0.3% and p_C = 0.9 ± 0.3% for the admixture containing 5% PX).

Chemical Shift Changes Associated with the Different Steps of the Interaction Trajectory. While the first step (A−B) of the three-state analysis reproduces features of the best-fit two-state model ($\Delta\omega_{AB}$, Figure S12, Supporting Information), $^{13}C'$ shifts associated with the second step ($\Delta\omega_{AC}$ measured relative to the free-state shifts) are ill defined for all sites, with the exception of the N and C termini of the helix (Figure S11, Supporting Information). For residues with pronounced $^{13}C'$ dispersion in the [PX]/[NT] = 0.05 data set, $\Delta\omega_{AC}$ values reproduce the $\Delta\omega_{AB}$ pattern (Figure S14, Supporting Information), indicating that the changes in $^{13}C'$ chemical shifts in the second step ($\Delta\omega_{BC}$) are close to zero. $^{13}C'$ shifts are highly sensitive to secondary structural propensity,[54] so that the first step is likely associated with a shift in helical population. The signs of the $^{13}C'$ shift changes were determined using previously established approaches,[55] revealing that helices are formed (positive $\Delta\omega$) in the A−B step, rather than removed (negative $\Delta\omega$), upon interaction (Table S1, Supporting Information).

The second step (B−C), occurring at a faster rate, affects mainly ^{15}N and $^{1}H^{N}$ RD measurements (Figure 6), with generally significantly larger $\Delta\omega$ than in the A−B step. In contrast to the ^{13}C shifts, $\Delta\omega$ values associated with the second step more closely resemble those observed in the two-state analysis (Figure S15, Supporting Information). Interestingly, the $^{1}H^{N}$ $\Delta\omega$ values appear to map the primary interaction site of NT with PX, with a pronounced helical periodicity observed along the sequence (Figure 6). Notably, the rate of this step closely corresponds to that of a known exchange process intrinsic to PX (k_{ex} = 2860 ± 160 s^{-1}) interpreted as a breathing motion of PX helices II and III.[56] We note that the presence of two distinct steps in the interaction process may also explain why

DOI: 10.1021/ja511066q
J. Am. Chem. Soc. 2015, 137, 1220−1229

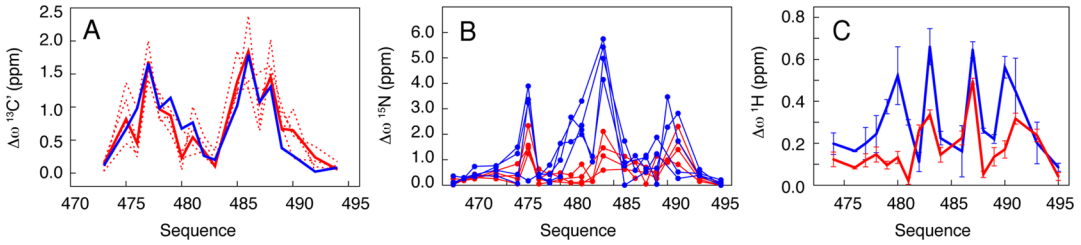

Figure 6. Chemical shift changes derived from the three-state exchange model for the NT:PX interaction shown in Figure 4. (A) Comparison of $\Delta\omega(^{13}C')$ derived from the three-state fits. $\Delta\omega_{AB}$ from independent admixtures (molar ratios 0.02, 0.035, 0.05, and 0.08, red dashed lines) and their weighted means (red solid line) are compared to $\Delta\omega_{AB}$ derived from analysis of all admixtures simultaneously (blue solid line). (B) Comparison of $\Delta\omega(^{15}N)$ derived from the three-state fit from molar ratio admixtures 0.02, 0.035, 0.05, and 0.08. $\Delta\omega_{AC}$ from independent admixtures (blue lines) compared to $\Delta\omega_{AB}$ from the same analysis (red lines). (C) Comparison of $\Delta\omega(^{1}H^{N})$ derived from the three-state fit. Weighted means and errors (blue line) of $\Delta\omega_{AC}$ derived from analysis of all admixtures, compared to weighted means of $\Delta\omega_{AB}$ (red line).

resonances of NT remain exchange broadened even in the presence of excess PX (Figure S5, Supporting Information).

Analysis of Conformational Changes Associated with the NT:PX Interaction. The fitted $^{13}C'$ $\Delta\omega$ values of NT derived from the three-state analysis were added to the free-state equilibrium isotropic $^{13}C'$ shifts to determine the chemical shifts in the B and C states. These values were then analyzed in terms of conformation using the minimum ensemble ASTEROIDS approach (see Experimental Section), initially assuming a single bound conformational state, and iteratively testing for the presence of more complex equilibria if simpler models did not adequately reproduce the data.[47,48] Comparison of the experimental shifts with values predicted from all possible helical ensembles spanning the entire molecular recognition element revealed that a single helix (476−489), strongly resembling the H2 helical state (476−488), is stabilized from the free-state equilibrium (Figure 7). No significant improvement in the data reproduction is achieved when invoking the presence of additional helices in exchange with this helix (Figure S16, Supporting Information). The first step of the interaction therefore appears to report on a population shift of NT from the free-state equilibrium to this single-helical state upon interaction with PX.

Characterization of the NT:PX Interaction from the Perspective of PX. ^{15}N and $^{1}H^{N}$ RD was also measured on the partner protein PX upon addition of NT (Figure S17, Supporting Information). In agreement with previous results,[56] we observe fast conformational exchange in several residues within helix III of free PX at a rate of k_{ex} = 2653 ± 654 s^{-1}. Titration of NT induces additional exchange occurring at a rate corresponding to those measured on NT for the first step of the interaction (803 ± 37 s^{-1} (Figures 2C and S18, Supporting Information)), with the residues involved mapping the interaction site of NT along the interhelical cleft of PX (Figure 7).

Estimation of Association Rates, Electrostatics, and Mutation Studies. The absence of RD in free NT indicates that already the first step of the three-state interaction model, with an exchange rate of $k_{ex,AB}$ = 852 ± 31 s^{-1} for the titration admixture with 5% PX, represents the initial binding interaction between NT and PX. At the protein concentrations used and based on the experimentally determined K_d of the interaction, this exchange rate corresponds to an association rate constant k_{on} of 9.7 × 10^{7} M^{-1} s^{-1} (see Experimental Section). This value significantly exceeds the diffusion limit[24] and indicates that electrostatic interactions play a role in initial complex formation. We tested this hypothesis by mutating the negatively charged residues D475 and D478 in the N-terminal part of the NT interaction region to alanines. The results show a slowing of the effective association rate to 4.4 × 10^{6} M^{-1} s^{-1}, supporting the suggestion that the initial encounter complex is electrostatically driven.

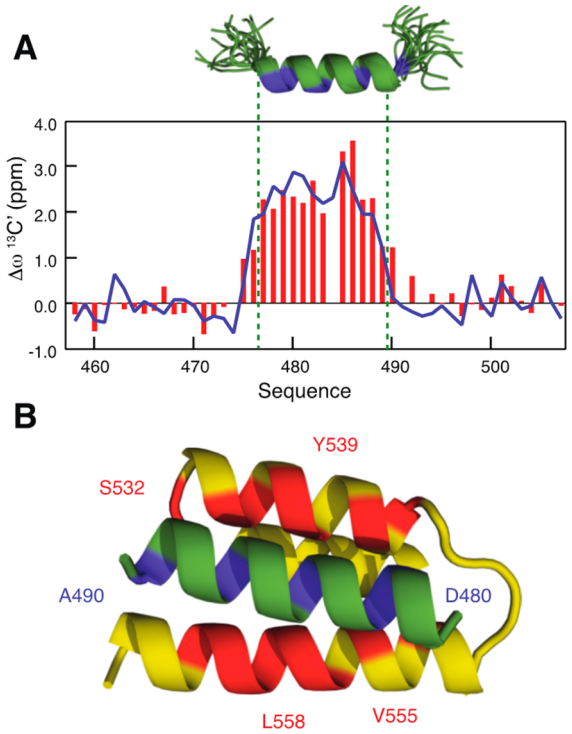

Figure 7. Structural analysis of the different steps of NT binding to PX. (A) $^{13}C'$ secondary chemical shifts of the bound state of NT (derived by adding $\Delta\omega_{AB}$ from the consensus three-state exchange model of Figure 4 to free-state shifts, red bars) and ASTEROIDS minimum ensemble selection against these shifts (blue line). A single ensemble substate, reporting on helix 476−489 populated to 100%, best reproduces the experimental data. The 476−489 helical subensemble is shown in cartoon representation above, corresponding closely to the H2 helix (476−488), populated to 28% in the free-state ensemble. Blue residues exhibit $\Delta\omega_{AC}(^{1}H^{N})$ values > 0.4 ppm. (B) Mapping the binding site of NT with PX. Ribbon representation of NT with sites showing $^{1}H^{N}$ RD derived shifts (blue) greater than the threshold ($\Delta\omega_{AC}(^{1}H^{N})$ > 0.4 ppm). Ribbon representation of PX shows the residues (red) displaying significant NT-induced ^{15}N or $^{1}H^{N}$ RD or significant shifts at all admixtures of NT. Numbers show positions of residues on PX (red) and NT (blue) exhibiting RD. The orientation of NT with respect to PX was optimized to agree with observed chemical shifts.

DISCUSSION

The high level of detail with which folding and binding events can be mapped using this combination of $^{13}C'$, ^{15}N, and $^{1}H^{N}$

DOI: 10.1021/ja511066q
J. Am. Chem. Soc. 2015, 137, 1220−1229

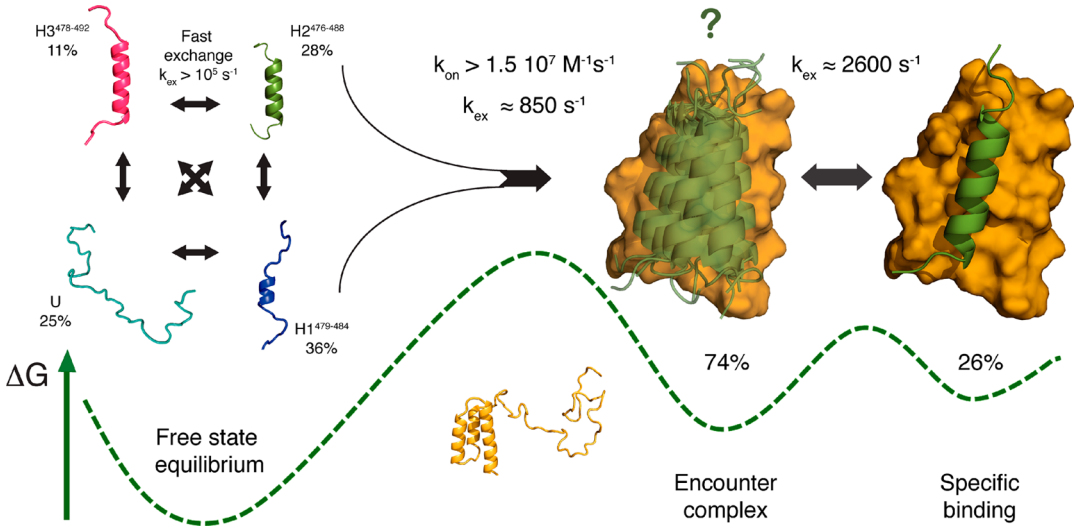

Figure 8. Proposed binding mechanism for Sendai virus NT to PX. Underlying conformational equilibrium in the free state, populating three helices (H1, H2, and H3, populations are shown for each helical ensemble) and the unfolded form (U), binds to PX via an initial encounter complex that repopulates the equilibrium by stabilizing a helix resembling H2 with a rate of 850 s^{-1}. Although the nature of the conformation of NT in the encounter complex is well described by the experimental data, its relative position with respect to PX is unknown in this step, although the global lack of significant ^{15}N and ^{1}H shifts associated with this step indicates that it is highly likely to be dynamic. This is indicated by the "fuzzy" nature of the cartoon in the intermediate step. The association rate of this step is estimated to be faster than the diffusion limit, indicating that this encounter complex is electrostatically driven, a prediction supported by mutation studies. Following the encounter, the helix locks into the PX binding site located in the helical groove on the surface of PX at a rate (2600 s^{-1}) coincident with intrinsic motions of the PX helices. A sketch of the free-energy landscape showing that the encounter step has a higher population than the second more specific step is shown. The on-rate limit is calculated on the basis of the highest estimated dissociation rate (60 μM), note that ITC suggests this is approximately 8.4 μM.

RD reveals a probable trajectory for formation of the NT:PX complex (Figure 8). According to this scenario, the interaction pathway follows a two-step process, initially funneling the existing conformational equilibrium[57] via stabilization of one of the interconverting helices known to be present in the free state.[47] This step accounts for the majority of RD-observed $^{13}C'$ chemical shifts, with minimal associated ^{15}N and $^{1}H^{N}$ shifts, suggesting that the initial interaction is nonspecific with respect to the surface of PX. Although the local conformation of NT (corresponding to helix H2) is well defined during the intermediate step, we have no information about the relative positioning of NT on the surface of PX. However, the mostly small ^{15}N and ^{1}H shifts associated with this step indicate that it is highly likely that this is a dynamic encounter complex. The second, faster step induces large ^{15}N and $^{1}H^{N}$ shifts, with the latter reporting on specific binding of one side of the NT helix in the interhelical groove on the surface of PX. Remarkably, the rate associated with this second step corresponds closely to the intrinsic conformational exchange rate observed in the helical groove of PX, providing strong evidence that the initial encounter complex is stabilized at a rate dictated by the intrinsic host protein dynamics.

This study thus provides experimental evidence of an IDP interaction mechanism comprising two distinct steps. The rapidly exchanging free-state equilibrium sampled by NT is repopulated upon initial encounter with PX, such that only one helix is present on the surface of PX. We note that from the experimental data alone we cannot distinguish whether stabilization of H2 occurs uniquely through binding of this helical state in a conformational selection-type mechanism or whether the individual states can each form H2 after encountering PX.[23,25] In either case the overall scenario is retained, consisting of funneling the initial conformational equilibrium into a state resembling H2 in the encounter complex. The final bound state is however not achieved via this initial encounter interaction, which remains nonspecific until the second binding event specifically locates NT into the helical groove on the surface of PX.

The possible thermodynamic advantages of formation of a nonspecific encounter complex facilitating subsequent localization in the specific partner binding site have been discussed extensively.[23,25,29] In the case of the NT:PX interaction, stabilization of the preformed helix presents the advantage that native contacts can be rapidly formed when the final interaction site is located on the surface of PX, a mechanism that is evidently energetically more favorable than complete folding upon binding from the disordered state. The first step, involving stabilization of an existing helical conformation, apparently incurs low enthalpic cost and is rather associated with a loss of entropy due to depopulation of the more disordered elements of the free state equilibrium. The second step is then driven by the enthalpic benefit associated with formation of specific interactions within the PX binding site.

Interestingly, NMR and stopped-flow studies of the intrinsically disordered ACTR protein that folds upon binding to its partner NCBD were used to demonstrate an acceleration of ligand binding as a function of intrinsic helical content,[58] in agreement with our observation that the helical population present in the free-state equilibrium of NT is important for binding. The atomic resolution conformational and thermodynamic analysis presented here provides a mechanistic framework for these observations. By contrast, time-resolved stopped-flow measurements, combined with circular dichroism and site-directed mutagenesis, recently indicated that residual structure is not required for binding of the disordered protein PUMA to its partner,[59] indicating rather the presence of a single-step, induced-fit type of mechanism. Our analysis of the NT:PX interaction however reveals a two-step process, the first of which

DOI: 10.1021/ja511066q
J. Am. Chem. Soc. 2015, 137, 1220−1229

clearly reports on the stabilization of one of the existing substates present in the free-state equilibrium of NT.

It is also important to note that analysis of only a subset of our experimental data, for example, ^{13}C RD curves alone or individual titration measurements, could be explained in terms of a two-state mechanism. However, the more complete data set clearly contradicts the simpler two-state models. Only the combination of $^{13}C'$, ^{15}N, and $^{1}H^{N}$ measurements identifies distinct steps, reporting predominantly on either folding ($^{13}C'$) or binding (^{15}N and $^{1}H^{N}$) events in the NT:PX interaction pathway. More generally, the intricate trajectory followed by this interaction further underlines the complexity of possible IDP binding mechanisms and reiterates the necessity for detailed atomic resolution studies to provide mechanistic explanations of experimental data.

CONCLUSION

Multinuclear RD provides an atomic resolution map of the molecular recognition trajectory of intrinsically disordered NT from the highly dynamic free-state equilibrium to the bound state, revealing a three-state interaction process whose binding modes and kinetics are regulated by the intrinsic dynamics of both proteins. This approach, providing high-resolution structural and kinetic information about a complex folding and binding interaction trajectory, can be applied to a number of experimental systems to provide a general framework for understanding conformational disorder in biomolecular function that will eventually inform rational drug intervention involving this enigmatic class of proteins.

EXPERIMENTAL SECTION

Sample Preparation. The NT domain comprising residues 401−524 of the nucleoprotein of Sendai virus (SeV) strain Harris, whose amino acid sequence corresponds to that of SeV Fushimi strain NT (UniProtKB accession number Q07097) except for the mutation E410K, as well as the PX domain comprising residues 474−568 of the phosphoprotein (UniProtKB P04859) of SeV strain Harris, were expressed and purified as described previously.[49] For preparation of NMR samples of ^{13}C,^{15}N isotope-labeled NT complexed with unlabeled PX, stock solutions of 208 μM ^{13}C,^{15}N-NT and 1.15 mM PX were used, both in 50 mM sodium phosphate buffer at pH 6.0 with 500 mM NaCl. The NT stock also contained 9.5% D_2O (v/v). From these stocks, admixtures of NT with 2%, 3.5%, 5%, 8%, and 15% PX (mol/mol) were made. Final NT:PX concentrations in these admixtures (in μM) were 204:4.1, 176:6.2, 199:9.9, 194:15.5, and 183:27.5, respectively. NMR experiments on free NT were recorded on a sample at a concentration of 305 μM. For samples of ^{15}N isotope-labeled PX alone or complexed with unlabeled NT, a stock solution of 408 μM ^{15}N-PX in 50 mM sodium phosphate, 500 mM NaCl, 1 mM DTT, and with 9.5% D_2O (v/v) at pH 6.0 was used. Appropriate amounts of a 286 μM stock solution of unlabeled NT (in 50 mM sodium phosphate, 500 mM NaCl, pH 6.0) were added to yield ^{15}N-PX samples with 5%, 8%, and 15% NT (mol/mol), respectively (final PX:NT concentrations (in μM) 378:18.8, 363:29, 331:49.6).

NMR Spectroscopy. NMR experiments were performed at sample temperatures of 25 °C on Varian/Agilent VNMRS 600 and 800 MHz spectrometers using room-temperature as well as cryogenically cooled triple-resonance HCN probes. All RD experiments employed constant-relaxation-time Carr−Purcell−Meiboom−Gill (CPMG) pulse schemes in which a series of 2D ^{15}N−^{1}H correlation spectra with different CPMG frequencies $\nu_{CPMG} = 1/(2\tau_{CP})$ were recorded, where τ_{CP} is the spacing between successive 180° refocusing pulses. Amide ^{15}N and $^{1}H^{N}$ as well as carbonyl $^{13}C'$ RD profiles were recorded using pulse sequences described in the literature.[60−62] In the ^{15}N RD experiment, ^{1}H continuous-wave decoupling was applied during the CPMG period. Typically, 10−14 points (including 1 or 2 duplicates for error analysis) were recorded for each dispersion curve, corresponding to ν_{CPMG} frequencies between 31.25 and 1000 Hz (^{15}N), 100 and 2000 Hz (^{1}H), and 66.7 and 933 Hz (^{13}C) at total constant-time relaxation delays (T_{relax}) of 32, 20, and 30 ms for ^{15}N, $^{1}H^{N}$, and $^{13}C'$ measurements, respectively. Spectra were usually acquired using sweep widths of 7.5 and 1.35 kHz as well as 512 and 120 complex points in ^{1}H and ^{15}N dimensions, respectively (at 600 MHz ^{1}H spectrometer frequency). To obtain the signs of chemical shift differences for ^{15}N, $^{1}H^{N}$, and $^{13}C'$ nuclei, HSQC (^{15}N, $^{1}H^{N}$) or HNCO ($^{13}C'$) spectra at different static magnetic fields were recorded as well as pairs of HSQC/HMQC spectra (^{15}N, $^{1}H^{N}$) and pairs of HNCO spectra with single- or multiple-quantum ^{15}N−^{13}CO coherence evolution ($^{13}C'$) at the same field.[55]

Data Analysis. Spectra were processed using NMRPipe[63] and analyzed in Sparky.[64] RD profiles ($R_{2,eff}(\nu_{CPMG})$) were calculated from peak heights according to $R_{2,eff}(\nu_{CPMG}) = -1/T_{relax}\ln(I(\nu_{CPMG})/I_0)$ with $I(\nu_{CPMG})$ being the peak height in the spectrum recorded with CPMG frequency ν_{CPMG} and I_0 the peak height in a reference spectrum recorded without a CPMG pulse train. Errors $\Delta R_{2,eff}$ in $R_{2,eff}$ values were calculated as $\Delta R_{2,eff}(\nu_{CPMG}) = \sigma/(T_{relax}\, I(\nu_{CPMG}))$ with σ being the pooled standard deviation of peak heights in duplicate measurements.[65]

RD curves were first analyzed using the software CATIA[53] (http://pound.med.utoronto.ca/~flemming/catia/) performing numerical integration of the Bloch−McConnell equations for a two-state exchange model. RD profiles from individual residues and nuclei measured at two static magnetic fields were fit assuming exchange (i.e., using CATIA) as well as assuming no exchange (i.e., to a constant value of $R_{2,eff}$). RD profiles were retained for further analysis if (a) assuming exchange improved the fit at the 99% confidence level according to F test statistics, (b) the difference between $R_{2,eff}$ values at minimum and maximum ν_{CPMG} values was at least 2 (^{15}N, ^{13}C) or 3 s^{-1} ($^{1}H^{N}$) at least at one static magnetic field, and (c) the average $\Delta R_{2,eff}$ error value of an RD profile was not larger than 25% at both static magnetic fields or not larger than 15% at least at one field. In the case of data recorded on labeled PX complexed with unlabeled NT, the presence of dispersion from fast exchange already in free PX[56] constitutes an additional complication. To analyze only RD processes related to NT binding, only such $R_{2,eff}$ profiles were retained that exhibited RD not present in the absence of NT or significantly different (as judged from fitting the $R_{2,eff}$ difference profile) from that present without NT.

All available RD curves originating from individual peptide planes (i.e., amide ^{15}N and $^{1}H^{N}$ data for residue i and carbonyl $^{13}C'$ data for residue $i-1$) retained as described above were then fit together for each peptide plane separately to yield residue-specific values of exchange rate constant k_{ex}, bound-state population p_B, chemical shift differences $\Delta\omega$ between free and bound state for the respective nuclei, and intrinsic transverse relaxation rate $R_{2,0}$ for each residue and nucleus at each field and each admixture. Further analysis of these RD profiles involved (a) fitting individual residues comprising data from all nuclei at all admixtures, assuming (residue-specific) k_{ex} and $\Delta\omega$ values to be constant across admixtures but allowing p_B to vary, using in-house software employing the analytical Carver−Richards equation,[66] (b) combined fitting of data from all nuclei and all residues at a given admixture of the two partner proteins to yield global (admixture-specific) values of k_{ex} and p_B using numerical integration by CATIA for two-state exchange, (c) combined fitting of all nuclei and all residues at a given admixture to a model of three-state exchange by way of numerical integration of the Bloch−McConnell equations using the software cpmg_fitd9[67] kindly provided by Dmitry Korzhnev, (d) combined fitting of all nuclei and all residues at NT admixtures with 2−8% PX to a model of linear three-state exchange, assuming constant values of k_{ex} and $\Delta\omega$ for the two exchange processes across different admixtures, but allowing p_B and p_C to vary with admixtures and $R_{2,0}$ to vary with each data set, by numerical integration of the Bloch−McConnell equations using home-written software, and finally (e) the program ChemEx[68] kindly provided by Guillaume Bouvignies was used to cross check results derived from a−d. Results were found to be entirely consistent between the different programs. The quality of fits was assessed using chi-squared statistics. Note that, in principle, the data might also be fit by forked three-state models; however, due to

DOI: 10.1021/ja511066q
J. Am. Chem. Soc. 2015, 137, 1220−1229

the more intuitive nature of a linear model allowing for a more straightforward interpretation in terms of structural and kinetic parameters, this avenue was not further pursued.

The parameter space for fits to dispersion data assuming three-state exchange is vast, comprises many local minima, and often exhibits correlations between parameters, such that different parameter sets can yield fits with similar chi-squared statistics. We narrowed down the space of possible solutions by first considering only the admixture of NT with 5% PX, for which the CPMG experiments yielded the best compromise between signal-to-noise and number of analyzable resonances on the one hand as well as dynamic range of $R_{2,\mathrm{eff}}$ values on the other. We initially required that the total excited-state population ($p_B + p_C$) did not exceed the relative amount of added binding partner (i.e., 5% in this case) and that no exchange rate in the resultant model exceeded 3000 s^{-1}. Convergence was obtained by fixing the sum of p_B and p_C to 5%, which given the precision of the fit is justified based on the measurement of K_d of the NT−PX interaction in the low micromolar range (Figure S2, Supporting Information). The resultant model of a three-state linear exchange has exchange rates of $k_{ex,AB} = 852 \pm 31$ s^{-1} and $k_{ex,BC} = 2600 \pm 493$ s^{-1} as well as excited-state populations of $p_B = 3.7 \pm 0.1\%$ and $p_C = 1.3 \pm 0.1\%$ (at the NT admixture with 5% PX). An extended grid search with less stringent requirements on resultant k_{ex} values (cutoff at 4000 s^{-1}, clearly above the sensitivity limit of CPMG experiments) consistently yielded a value of $k_{ex,AB}$ in the range of the k_{ex} found in two-state fits as well as $^{13}C'$ chemical shift changes between states A and B corresponding to those extracted from two-state fits, as is the case for the three-state model described above. We then tested the validity of this minimum by fixing $k_{ex,AB}$ to 850 s^{-1} and fitting populations, chemical shifts, and $k_{ex,BC}$ as free parameters. This again localized a global minimum over the resultant parametric space in the combination $k_{ex,AB}$, $k_{ex,BC}$ (850 s^{-1}, 2650 s^{-1}) and p_B, p_C (3.5%, 1.5%).

On the basis of the absence of RD and the fast interconversion of different helical conformers in free NT, we judged the first (A−B) of the two steps of this mechanism, with an exchange rate of 852 ± 31 s^{-1}, to correspond to the bimolecular binding reaction between NT and PX. Using the concentration of free PX ligand [P] in the 5% PX admixture of NT, calculated based on the K_d of the interaction of 8.4 μM measured by ITC (see below), the association rate constant k_{on} can be calculated as $k_{on} = k_{ex}/([P] + K_d)$, yielding a value of 9.7×10^7 M^{-1} s^{-1}. The corresponding dissociation rate constant k_{off} amounts to 811 s^{-1}. Exchange rates $k_{ex,AB}$ for the other NT:PX admixtures (containing 2%, 3.5%, 8%, and 15% PX, respectively) were calculated based on these k_{on} and k_{off} values and the corresponding concentrations of free PX, yielding values of 827, 839, 879, and 948 s^{-1}, respectively. The rate of the unimolecular second step of the three-state model ($k_{ex,BC} = 2600 \pm 493$ s^{-1}) was assumed to remain constant. Using this exchange model, dispersion data at all admixtures yielded very good fits (with $k_{ex,AB}$ and $k_{ex,BC}$ fixed) based on chi-squared statistics (Table 1) and resulted in p_B and p_C values in the range expected from the K_d of the interaction (Figure 5).

To obtain $\Delta\omega$ values also for those residues of the PX binding site of NT whose RD curves did not meet the significance criteria described above, we ran fits (assuming two- and three-state exchange) to data from all residues of this region, fixing global parameters (k_{ex} and p_B for two-state exchange, $k_{ex,AB}$, $k_{ex,BC}$, p_B, p_C for three-state exchange) to the values obtained using only CPMG data exhibiting significant RD, for each admixture separately.

Signs of chemical shift differences for ^{13}C nuclei (assuming two-state exchange) were obtained by comparing resonance positions in pairs of HNCO spectra with single- or multiple-quantum $^{15}N-^{13}CO$ coherence evolution (^{13}C)[55] and in spectra containing different amounts of unlabeled partner protein. The visible resonance is expected to be closer to the excited-state resonance peak in the single-quantum spectrum and in the spectrum with a larger amount of binding partner, respectively. Chemical shift differences were considered significant if their absolute value exceeded the mean plus one standard deviation of all chemical shift differences between corresponding peaks; in addition, shift differences smaller than 1 Hz were not considered significant.

Ensemble Calculations Using ASTEROIDS. In order to model the conformational ensemble of NT when bound to PX, we applied the minimum ensemble approach[47] implemented in a version of the ASTEROIDS genetic algorithm for ensemble selection,[69−71] with NT $^{13}C'$ shifts in complex as selection criteria.[48,72] $^{13}C'$ shifts of PX-complexed NT were generated as the sum of free-state $^{13}C'$ chemical shifts and $^{13}C'\Delta\omega_{AB}$ values as obtained from the model of three-state exchange fitting best to RD data ($k_{ex,AB} = 852 \pm 31$ s^{-1} and $k_{ex,BC} = 2600 \pm 493$ s^{-1} for NT with 5% PX). Weighted means over $^{13}C'$ $\Delta\omega_{AB}$ values from individual admixtures were used. A common empirical correction of −0.25 ppm was applied to all free-state $^{13}C'$ NT chemical shifts following calibration of ASTEROIDS ensemble selection against the free-state $^{13}C'$ shifts compared to the known total helical content of the central binding site of free NT (75% in residues 479−484).[47]

We used an existing flexible-meccano[73,74] ensemble of NT conformers containing subensembles for all possible helices (4−20 residues in length) covering residues 476−495 as well as a fully unfolded subensemble, yielding a total of 154 subensembles with 1000 conformers each.[47] Chemical shifts were calculated for all conformers using SPARTA[75] and averaged over subensembles. ASTEROIDS was run to obtain the weighted combination of unfolded and helical ensembles yielding the best fit to the experimental $^{13}C'$ chemical shift data for increasing numbers of helical conformers ($n = 1, 2, 3, 4$), similar to the approach using residual dipolar coupling data as described.[47] Each helical conformer thus introduced three parameters into the fit (helix start, end, and population). The data could well be fit assuming a single helix extending between residues 476 and 489, very similar to helix H2 of the free state,[47] populated to 100%. No improvement ($p > 0.1$) was obtained with ensembles with more helical contributions or with a population of an unfolded conformer.

Analysis of Mutational Studies of NT:PX Interaction. In order to perturb the observed interaction kinetics in a controlled way, two key mutations were made to NT, replacing Asp475 and Asp478 by alanines. ^{15}N, $^{1}H^{N}$, and $^{13}C'$ RD measurements were made at concentrations of mutant NT of 190 μM and PX of 6.7 μM (0.035 molar ratio of PX) and compared to those measured using wild-type NT. Two-state global fits to all residues and nuclei of mutant NT showing dispersion yielded an exchange rate $k_{ex} = 247 \pm 33$ s^{-1} and a bound state population of $p_B = (2.7 \pm 0.3)\%$. This value of p_B would correspond to a K_d of 55 μM (calculated as $K_d = (1 - p_B)\cdot([P_0]/p_B - [N_0])$, with $[P_0]$ and $[N_0]$ being the total concentrations of PX and NT, respectively). Using this K_d estimate to calculate the concentration of free PX ligand [P], an estimate of k_{on} can be calculated from k_{ex} as described above, yielding a value of 4.4×10^6 M^{-1} s^{-1} for the NT mutant.

Isothermal Titration Calorimetry. ITC measurements were performed on the MicroCal iTC200 (GE Healthcare, PA) at 25 °C. Prior to the experiment, the proteins were dialyzed into the same ITC buffer (50 mM sodium phosphate pH 6.0, 500 mM NaCl, 2 mM β-mercaptoethanol). PX at a concentration of 750 μM was titrated into a solution of NT at a concentration of 50 μM. A total of 24 injections of 1.5 μL were performed every 180 s at a stirring speed of 800 rpm. Data were analyzed using Origin (OriginLab, Northampton, MA) and yielded a dissociation constant of 8.4 ± 0.9 μM.

■ ASSOCIATED CONTENT

Supporting Information

Spectra of NT and PX alone and in the presence of their respective partner protein; ITC binding isotherm for the NT:PX interaction; ^{1}H, ^{13}C, and ^{15}N relaxation dispersion curves from NT and PX free and in complex with substoichiometric mixtures of the partner protein; figures showing results of different data fitting procedures; table containing the signs of the RD-measured $^{13}C'$ chemical shift changes in NT. This material is available free of charge via the Internet at http://pubs.acs.org.

■ AUTHOR INFORMATION

Corresponding Author

*E-mail: martin.blackledge@ibs.fr.

DOI: 10.1021/ja511066q
J. Am. Chem. Soc. 2015, 137, 1220−1229

Present Address

[‖]Université Lille 1, UMR CNRS 8576, Cité Scientifique, Bât. C9, 59655 Villeneuve d'Ascq Cedex, France.

Notes

The authors declare no competing financial interest.

■ ACKNOWLEDGMENTS

This work was funded by the Agence Nationale de Recherche under ComplexDynamics (SIMI7, M.B.) and ProteinDisorder (JCJC, M.R.J.) and by the Human Frontier Science Program (long-term fellowship LT000322/2011-L to R.S.). D.F.H. is a BBSRC David Phillips Fellow.

■ REFERENCES

(1) Dyson, H. J.; Wright, P. E. *Nat. Rev. Mol. Cell Biol.* **2005**, *6*, 197.
(2) Dunker, A. K.; Silman, I.; Uversky, V. N.; Sussman, J. L. *Curr. Opin. Struct. Biol.* **2008**, *18*, 756.
(3) Tompa, P. *Curr. Opin. Struct. Biol.* **2011**, *21*, 419.
(4) Dunker, A. K.; Uversky, V. N. *Nat. Chem. Biol.* **2008**, *4*, 229.
(5) Davey, N. E.; Travé, G.; Gibson, T. J. *Trends Biochem. Sci.* **2011**, *36*, 159.
(6) Babu, M. M.; Kriwacki, R. W.; Pappu, R. V. *Science* **2012**, *337*, 1460.
(7) Van Roey, K.; Gibson, T. J.; Davey, N. E. *Curr. Opin. Struct. Biol.* **2012**, *22*, 378.
(8) Tompa, P.; Davey, N. E.; Gibson, T. J.; Babu, M. M. *Mol. Cell* **2014**, *55*, 161.
(9) Babu, M. M.; van der Lee, R.; de Groot, N. S.; Gsponer, J. *Curr. Opin. Struct. Biol.* **2011**, *21*, 432.
(10) Jensen, M. R.; Ruigrok, R. W.; Blackledge, M. *Curr. Opin. Struct. Biol.* **2013**, *23*, 426.
(11) Esteban-Martín, S.; Fenwick, R. B.; Salvatella, X. *J. Am. Chem. Soc.* **2010**, *132*, 4626.
(12) Fisher, C. K.; Huang, A.; Stultz, C. M. *J. Am. Chem. Soc.* **2010**, *132*, 14919.
(13) Allison, J. R.; Varnai, P.; Dobson, C. M.; Vendruscolo, M. *J. Am. Chem. Soc.* **2009**, *131*, 18314.
(14) Forman-Kay, J. D.; Mittag, T. *Structure* **2013**, *21*, 1492.
(15) Mantsyzov, A. B.; Maltsev, A. S.; Ying, J.; Shen, Y.; Hummer, G.; Bax, A. *Protein Sci.* **2014**, *23*, 1275.
(16) Jensen, M. R.; Zweckstetter, M.; Huang, J.; Blackledge, M. *Chem. Rev.* **2014**, *114*, 6632.
(17) Sugase, K.; Dyson, H. J.; Wright, P. E. *Nature* **2007**, *447*, 1021.
(18) Mittag, T.; Marsh, J.; Grishaev, A.; Orlicky, S.; Lin, H.; Sicheri, F.; Tyers, M.; Forman-Kay, J. D. *Structure* **2010**, *18*, 494.
(19) Wang, Y.; Fisher, J. C.; Mathew, R.; Ou, L.; Otieno, S.; Sublet, J.; Xiao, L.; Chen, J.; Roussel, M. F.; Kriwacki, R. W. *Nat. Chem. Biol.* **2011**, *7*, 214.
(20) Krishnan, N.; Koveal, D.; Miller, D. H.; Xue, B.; Akshinthala, S. D.; Kragelj, J.; Jensen, M. R.; Gauss, C.-M.; Page, R.; Blackledge, M.; Muthuswamy, S. K.; Peti, W.; Tonks, N. K. *Nat. Chem. Biol.* **2014**, *10*, 558.
(21) Oldfield, C. J.; Meng, J.; Yang, J. Y.; Yang, M. Q.; Uversky, V. N.; Dunker, A. K. *BMC Genomics* **2008**, *9* (Suppl 1), S1.
(22) Tompa, P.; Szász, C.; Buday, L. *Trends Biochem. Sci.* **2005**, *30*, 484.
(23) Csermely, P.; Palotai, R.; Nussinov, R. *Trends Biochem. Sci.* **2010**, *35*, 539.
(24) Kjaergaard, M.; Teilum, K.; Poulsen, F. M. *Proc. Natl. Acad. Sci. U.S.A.* **2010**, *107*, 12535.
(25) Kiefhaber, T.; Bachmann, A.; Jensen, K. S. *Curr. Opin. Struct. Biol.* **2012**, *22*, 21.
(26) Dogan, J.; Gianni, S.; Jemth, P. *Phys. Chem. Chem. Phys.* **2014**, *16*, 6323.
(27) Tompa, P.; Fuxreiter, M. *Trends Biochem. Sci.* **2008**, *33*, 2.
(28) Frauenfelder, H.; Sligar, S.; Wolynes, P. *Science* **1991**, *254*, 1598.
(29) Shoemaker, B. A.; Portman, J. J.; Wolynes, P. G. *Proc. Natl. Acad. Sci. U.S.A.* **2000**, *97*, 8868.
(30) Motlagh, H. N.; Hilser, V. J. *Proc. Natl. Acad. Sci. U.S.A.* **2012**, *109*, 4134.
(31) Liu, J.; Faeder, J. R.; Camacho, C. J. *Proc. Natl. Acad. Sci. U.S. A.* **2009**, *106*, 19819.
(32) Long, D.; Brüschweiler, R. *Plos Comput. Biol.* **2011**, *7*, e1002035.
(33) Knott, M.; Best, R. B. *PLoS Comput. Biol.* **2012**, *8*, e1002605.
(34) Ganguly, D.; Chen, J. *J. Am. Chem. Soc.* **2009**, *131*, 5214.
(35) Zhang, W.; Ganguly, D.; Chen, J. *PLoS Comput. Biol.* **2012**, *8*, e1002353.
(36) Bachmann, A.; Wildemann, D.; Praetorius, F.; Fischer, G.; Kiefhaber, T. *Proc. Natl. Acad. Sci. U.S.A.* **2011**, *108*, 3952.
(37) Rogers, J. M.; Steward, A.; Clarke, J. *J. Am. Chem. Soc.* **2013**, *135*, 1415.
(38) Ferreon, A. C. M.; Ferreon, J. C.; Wright, P. E.; Deniz, A. A. *Nature* **2013**, *498*, 390.
(39) Wright, P. E.; Dyson, H. J. *Curr. Opin. Struct. Biol.* **2009**, *19*, 31.
(40) Palmer, A. *Chem. Rev.* **2004**, *104*, 3623.
(41) Baldwin, A. J.; Kay, L. E. *Nat. Chem. Biol.* **2009**, *5*, 808.
(42) Wishart, D. S.; Sykes, B. D. *J. Biomol. NMR* **1994**, *4*, 171.
(43) Gerard, F. C. A.; Ribeiro, E. de A., Jr; Leyrat, C.; Ivanov, I.; Blondel, D.; Longhi, S.; Ruigrok, R. W. H.; Jamin, M. *J. Mol. Biol.* **2009**, *388*, 978.
(44) Communie, G.; Ruigrok, R. W.; Jensen, M. R.; Blackledge, M. *Curr. Opin. Virol.* **2014**, *5*, 72.
(45) Curran, J.; Homann, H.; Buchholz, C.; Rochat, S.; Neubert, W.; Kolakofsky, D. *J. Virol.* **1993**, *67*, 4358.
(46) Serrano, L.; Fersht, A. R. *Nature* **1989**, *342*, 296.
(47) Jensen, M. R.; Houben, K.; Lescop, E.; Blanchard, L.; Ruigrok, R. W. H.; Blackledge, M. *J. Am. Chem. Soc.* **2008**, *130*, 8055.
(48) Jensen, M. R.; Salmon, L.; Nodet, G.; Blackledge, M. *J. Am. Chem. Soc.* **2010**, *132*, 1270.
(49) Houben, K.; Marion, D.; Tarbouriech, N.; Ruigrok, R. W. H.; Blanchard, L. *J. Virol.* **2007**, *81*, 6807.
(50) Kingston, R. L.; Hamel, D. J.; Gay, L. S.; Dahlquist, F. W.; Matthews, B. W. *Proc. Natl. Acad. Sci. U.S.A.* **2004**, *101*, 8301.
(51) Bourhis, J.-M.; Receveur-Bréchot, V.; Oglesbee, M.; Zhang, X.; Buccellato, M.; Darbon, H.; Canard, B.; Finet, S.; Longhi, S. *Protein Sci.* **2005**, *14*, 1975.
(52) McConnell, H. M. *J. Chem. Phys.* **1958**, *28*, 430.
(53) Hansen, D. F.; Vallurupalli, P.; Lundström, P.; Neudecker, P.; Kay, L. E. *J. Am. Chem. Soc.* **2008**, *130*, 2667.
(54) Wang, Y.; Jardetzky, O. *J. Am. Chem. Soc.* **2002**, *124*, 14075.
(55) Skrynnikov, N. R.; Dahlquist, F. W.; Kay, L. E. *J. Am. Chem. Soc.* **2002**, *124*, 12352.
(56) Houben, K.; Blanchard, L.; Blackledge, M.; Marion, D. *Biophys. J.* **2007**, *93*, 2830.
(57) Wang, J.; Oliveira, R. J.; Chu, X.; Whitford, P. C.; Chahine, J.; Han, W.; Wang, E.; Onuchic, J. N.; Leite, V. B. P. *Proc. Natl. Acad. Sci. U.S.A.* **2012**, *109*, 15763.
(58) Iesmantavicius, V.; Dogan, J.; Jemth, P.; Teilum, K.; Kjaergaard, M. *Angew. Chem., Int. Ed.* **2014**, *53*, 1548.
(59) Rogers, J. M.; Wong, C. T.; Clarke, J. *J. Am. Chem. Soc.* **2014**, *136*, 5197.
(60) Hansen, D. F.; Vallurupalli, P.; Kay, L. E. *J. Phys. Chem. B* **2008**, *112*, 5898.
(61) Ishima, R.; Torchia, D. A. *J. Biomol. NMR* **2003**, *25*, 243.
(62) Lundström, P.; Hansen, D. F.; Kay, L. E. *J. Biomol. NMR* **2008**, *42*, 35.
(63) Delaglio, F.; Grzesiek, S.; Vuister, G.; Zhu, G.; Pfeifer, J.; Bax, A. *J. Biomol. NMR* **1995**, *6*, 277.
(64) Goddard, T.; Kneller, D. *SPARKY 3*; University of California, San Francisco.
(65) Ishima, R.; Torchia, D. A. *J. Biomol. NMR* **2005**, *32*, 41.
(66) Carver, J.; Richards, R. *J. Magn. Reson.* **1972**, *6*, 89.
(67) Korzhnev, D. M.; Neudecker, P.; Mittermaier, A.; Orekhov, V. Y.; Kay, L. E. *J. Am. Chem. Soc.* **2005**, *127*, 15602.

DOI: 10.1021/ja511066q
J. Am. Chem. Soc. 2015, 137, 1220−1229

(68) Vallurupalli, P.; Bouvignies, G.; Kay, L. E. *J. Am. Chem. Soc.* **2012**, *134*, 8148.
(69) Nodet, G.; Salmon, L.; Ozenne, V.; Meier, S.; Jensen, M. R.; Blackledge, M. *J. Am. Chem. Soc.* **2009**, *131*, 17908.
(70) Salmon, L.; Nodet, G.; Ozenne, V.; Yin, G.; Jensen, M.; Zweckstetter, M.; Blackledge, M. *J. Am. Chem. Soc.* **2010**, *132*, 8407.
(71) Ozenne, V.; Schneider, R.; Yao, M.; Huang, J.-R.; Salmon, L.; Zweckstetter, M.; Jensen, M. R.; Blackledge, M. *J. Am. Chem. Soc.* **2012**, *134*, 15138.
(72) Kragelj, J.; Ozenne, V.; Blackledge, M.; Jensen, M. R. *ChemPhysChem* **2013**, *14*, 3034.
(73) Bernadó, P.; Blanchard, L.; Timmins, P.; Marion, D.; Ruigrok, R. W. H.; Blackledge, M. *Proc. Natl. Acad. Sci. U.S.A.* **2005**, *102*, 17002.
(74) Ozenne, V.; Bauer, F.; Salmon, L.; Huang, J.-R.; Jensen, M. R.; Segard, S.; Bernadó, P.; Charavay, C.; Blackledge, M. *Bioinformatics* **2012**, *28*, 1463.
(75) Shen, Y.; Bax, A. *J. Biomol. NMR* **2007**, *38*, 289.

DOI: 10.1021/ja511066q
J. Am. Chem. Soc. 2015, 137, 1220−1229